1 **Phosphorus solubility in basaltic glass: limitations for phosphorus immobilization in glass**

2 **and glass-ceramics**

3

4 M. Tarrago[1,2], M. Garcia-Valles[1], S. Martínez[1], D.R. Neuville[2]

5 [1]*Dept. Mineralogia, Petrologia i Geologia Aplicada, Facultat de Ciències de la Terra.*

6 *Universitat de Barcelona, c/ Martí i Franquès, s/n, 08028 Barcelona.*

7 [2]*CNRS-Institut de Physique du Globe de Paris, USPC, 1 rue Jussieu 75005 Paris, France*

8

9 Corresponding author : M. Tarrago (mtarrago@ub.edu; tarrago@ipgp.fr)

10

11 **Abstract**

12   The composition of sewage sludge from urban wastewater treatment plants is simulated

13 using P-doped basalts. Electron microscopy analyses show that the solubility of P in the basaltic

14 melt is limited by the formation of a liquid-liquid immiscibility in the form of an aluminosilicate

15 phase and a Ca-Mg-Fe-rich phosphate phase. The rheological behavior of these compositions is

16 influenced by both phase separation and nanocrystallization. Upon a thermal treatment, the

17 glasses will crystallize into a mixture of inosilicates and spinel-like phases at low P contents and

18 into Ca-Mg-Fe phosphate at high P contents. Hardness measurements yield values between

19 5.41-7.66 GPa, inside the range of commercial glasses and glass-ceramics. Leaching affects

20 mainly unstable Mg^{2+}-PO_4^{3-} complexes.

21

24

25 **1. Introduction**

26   Vitrification is a widespread inertization technique that can be applied to the remediation of

27 both hazardous and non-hazardous wastes to reduce the volume of the disposal material (and

28 thus the necessity of landfills) and to immobilize the toxic elements of the raw waste in the glass

29   structure. Several examples of inertization by this approach can be found in the literature:

30   polluted soils (Careghini et al., 2010; Navarro et al., 2013), radioactive wastes (Ciecińska et al.,

31   2015; Davydov et al., 1996; Hrma et al., 2014; Pioro et al., 2001), incineration ashes (Cheng,

32   2004; Cheng et al., 2002; Haugsten and Gustavson, 2000; Jung et al., 2005; Kavouras et al.,

33   2003; Romero et al., 2001). The production of glass-ceramics from these glasses enables further

34   inertization due to the emplacement of toxic elements in the structure of minerals (Binhussain et

35   al., 2014; Garcia-Valles et al., 2007; Mymrin et al., 2014; Varitis et al., 2015). The glass-

36   ceramic process also provides recycled materials with superior mechanical properties (Marinoni

37   et al., 2013; Teixeira et al., 2014). These glasses and glass-ceramics – apart from those made

38   using radioactive wastes – may have applications in the building industry such as pavements or

39   wall covers (Romero and Rincón, 1997).

40   Sewage sludges (SS) from urban wastewater treatment plants (UWWTP) have a good

41   potential as one of the raw materials for an inertization matrix because their compositions are

42   roughly similar to that of basalt (Rincon, 2016) (Table 1). This matrix could be tested to host

43   contaminant and hazardous wastes like galvanic sludge (Garcia-Valles et al., 2007). However,

44   the higher abundance of some elements, such as phosphorus and calcium, in the sludge

45   compared to basalts or any natural igneous system requires experimental studies to understand

46   how the compositional variation affects their properties and their long-term stability.

47   Phosphorus is an essential nutrient, as it is present in the structure of several biomolecules

48   such as DNA or RNA, in cell membranes, and in the inorganic fraction of bone. Low phosphate

49   levels limit the growth in both terrestrial and aquatic systems, hence the amount of soil

50   phosphate has long been complemented using fertilizers. Sewage sludge may be a substitute for

51   these (European Council, 1986). However, an exceeding amount of phosphorus may cause two

52   environmental issues:

53   1. Euthrophication: excessive growth of algae and aquatic plants due to a great supply

54   of nutrients resulting in oxygen overconsumption and depletion. Hypoxic conditions

55   cause animal death and stop biological purification of water (Correll, 1998; Werner,

56   2012). It is considered the greatest threat for surface waters worldwide.

57   2. Heavy metal input in the soil due to high Cd contents in fertilizers (Werner, 2012).

58   The application of sewage sludge in agriculture is then limited and requires additional recycling

59   methods (Mininni et al., 2015).

60   In rock-forming silicate melts, the effect of phosphorus on both melt structure and properties

61   is considered of great importance despite its scarcity (natural igneous melts usually have less

62   than 1 wt% P_2O_5) because it has a strong influence on phase relationships, physical and

63   chemical properties (Dupree et al., 1989; Gan and Hess, 1992; Mysen et al., 1981; Ryerson and

64   Hess, 1980; Toplis et al., 1994; Wyllie and Tuttle, 1964). Even small amounts of P_2O_5 may

65   cause structural variations in the liquid that alter the values of the trace-element partition

66   coefficient by tenths percent (Ryerson and Hess, 1978). The addition of phosphorus to silicate

67   melts is known to influence a number of properties and processes, including the redox state of

68   iron, viscosity and density (Toplis et al., 1994), the formation of an immiscibility gap (Wyllie

69   and Tuttle, 1964), the shifts of the liquidus boundary of the silicate minerals, an increase in the

70   silica activity coefficient and the expansion of the liquid immiscibility volume (Ryerson and

71   Hess, 1980).

72   This paper focuses on the addition of phosphorus to basalt to simulate the inertization of

73   sewage sludge, an appropriate glass-making composition due to its low viscosity at high

74   temperature (<1300°C). The amount of P that may be bound in basalt is established by

75   determining its solubility in the melt together with an analysis of the structure, thermal

76   evolution, rheological behavior, and macroscopic properties in order to constrain the production

77   process. The obtained materials underwent hardness and chemical resistance tests to establish

78   potential uses.

79

80

81   **2. Experimental methods**

82   2.1. Choice of compositional range

83   The chemical compositions of a series of sewage sludge (SS) from wastewater treatment

84   plants (WWTP) and a basalt from Sant Joan les Fonts (Girona, Catalonia) (Table 1) have been

85   analyzed by X-ray fluorescence (XRF), using a sequential X-ray spectrophotometer Phillips

86   PW2400. The range of phosphorus concentration in sewage sludge has been complemented with

87   data from the literature (Borowski et al., 2014; Folgueras et al., 2003; Forsberg and Ledin,

88   2006; Hossain et al., 2009; Kikuchi, 1998; Montero et al., 2009; Roig et al., 2012; Wang et al.,

89   2008). Its maximum is 32.98 wt% P_2O_5 (Wang et al., 2008).

90

91   2.2. Glass production

92   A basaltic rock of La Garrotxa (Girona, Catalonia) is doped with $NH_4H_2PO_4$ (ADHP, Reag-

93   Ph.Eur, PA-ACS 131126.1211) to simulate a SS-like matrix. The mixtures are homogenized in

94   a ball mill for 30 min and melted in a Pt-Rh crucible placed inside a globular alumina furnace

95   equipped with SuperKanthal™ heating elements and an Eurotherm® 902 programmer. Each

96   sample is heated at 200 ºC for 2 h to decompose the ADHP and then above the melting point at

97   1450 ºC, for 4h. Part of the quenched glass has been annealed for 12 h at 500 ºC.

98   Some mg of each glass have been remelted at 1450ºC and 1600ºC using a Pt-Rh alloy wire

99   heating system originally designed to obtain spectroscopic data of silicate melts at high

100 temperatures (Mysen and Frantz, 1992; Neuville and Mysen, 1996; Neuville et al., 2014b). The

101 wires have previously been calibrated using salts with known melting points in order to achieve

102 reliable determination of temperature.

103

104 2.3. Electron microscopy

105 Textural information and qualitative punctual chemical analysis of the glasses and the

106 crystalline phases formed during production have been obtained using a JEOL J-7100 field

107 emission scanning electron microscope with EDS detector and backscattered electron detector

108 (FE-SEM-EDS). A thin section of the sample most enriched in P (labeled B32P) has been

109 analyzed using a Hitachi H-800-MT transmission electron microscope (TEM) with energy

110 dispersed analysis of X-rays (EDX), operating at 200 kV in STEM mode using the dark field

111 detector. The beam size used in this mode is around 15 nm. The spectrometer is an Oxford

112 Instruments INCA x-sight, with Si (Li) detector. The map acquisition is accomplished using the

INCA Microanalysis Suite, software version 4.09. X-ray maps are obtained selecting the characteristic X-ray peaks for Si, Al, Ca, Fe, Mg and P.

2.4. Density measurements

The densities of glass fragments are measured with the Archimedean method using toluene as the immersion liquid. The masses of several glass fragments are measured in air (M_a) and in toluene (M_t). The variation in the density of toluene, ρT, is corrected using the temperature T of toluene and its equation of state. The density of the glasses is calculated using the following equation $\rho = M_a * \rho T / (M_a - M_t)$.

2.5. Raman spectroscopy

Raman spectra are obtained using a T64000 Jobin-Yvon Raman spectrometer equipped with a CCD detector. The light source is an Ar^+ ion laser operating at 488 nm with a typical output of 100 mW on the sample. The integration time is 300 s and the spectral range is between 100 – 1500 cm^{-1}. The spectra are treated with the Long correction (Long, 1977; Neuville et al., 2014b) and normalized to the total area.

2.6. Thermal Analysis

Crystallization temperatures during thermal treatments have been determined using Differential Thermal Analysis (DTA) in a Netzsch STA 409 vertical furnace. The experiments have been performed using Pt-Rh crucibles in air, with a flow rate of 80 mL/min and a heating rate of 10ºC/min from room temperature to 1300ºC followed by free cooling. The reference material is aluminum oxide 0419-0197 from Perkin Elmer.

2.7. X-Ray diffraction

X-Ray diffraction has been used both to assess the amorphous character of the glasses right after production and to determine which phases crystallize during thermal treatments. X-Ray diffraction spectra have been obtained from powdered samples (particles under 45 µm) in a

141 Bragg-Brentano PANAnalytical X'Pert Diffractometer system (graphite monochromator,

142 automatic gap, Kα-radiation of Cu at λ = 1.54061 Å, powered at 45 kV – 40 mA, scanning

143 range 4 – 100º with a 0.017º 2θ step scan and a 50 s measuring time). Identification and

144 semiquantitative evaluation of phases has been made on PANanalytical X'Pert HighScore

145 software.

146

147 2.8. Dilatometry

148 Glass transition temperature (Tg) has been obtained by dilatometry in a Linseis L76/1550

149 horizontal dilatometer. 20 mm long bars were cut from each glass, then placed in the sample

150 carrier and heated up to around 750ºC at 10ºC/min. When samples are too viscous to be cast

151 into bars the analysis is performed in powdered glass, inside a SP5856/3605/10 sample carrier.

152 A value of 10^{12} Pa·s has been assigned to Tg (Yue, 2008).

153

154 2.9. Hot-stage microscopy

155 The temperatures of the fixed viscosity points (Pascual et al., 2001) for Hot-Stage

156 Microscopy (HSM) are determined by optical observation of the deformation of 3 mm-high test

157 tube conformed using powdered glass (<45 μm) bound in a uniaxial press using a 1/20 solution

158 of Elvacite®. Test tubes have been heated at 5ºC/min up to 1450ºC in air. The process is

159 recorded with ProgRes Capture Pro software and the picture analysis has been performed using

160 Hot-stage software (Garcia-Valles et al., 2013). The error in the determination of temperature

161 using this method is ± 10 ºC (Pascual et al., 2001).

162

163 2.10. Microhardness

164 The microhardness of the samples has been measured on polished glass probes using a

165 Galileo Isoscan OD Vickers micro-indenter with a load of 300 g.

166

167 2.11. Leaching tests

168   The elementary analysis of the leachates has been used to evaluate the stability of the glasses

169   according to DIN 38414-S4 (DIN-38414S4, 1984). The test has been performed in 10 g of dried

170   sample (particle size between 2 and 4 mm), mixed in 100 mL of deionized water. The mixture is

171   agitated in a rotating shaker at room temperature during 24 h and the liquid is separated from

172   the solid using a 0.45 µm pore size filter. The leachates have been analyzed by inductively

173   coupled plasma optical emission spectrometry (ICP-OES, Optima 3100×, PerkinElmer) and

174   inductively coupled plasma mass spectrometry (ICP-MS, Elan 6000, PerkinElmer).

175

176   **3. Results**

177   3.1. Sewage sludge compositions

178   The chemical compositions of a series of sewage sludge from UWWTP are presented in

179   Table 1. The main components of the sludge are Al_2O_3, SiO_2, CaO, Fe_2O_3 and P_2O_5. The high

180   amount of P – common in urban sewage sludge – is due to the predominance of porcine farming

181   in the source area. The abundance of Al_2O_3, SiO_2 and Fe_2O_3 supports the use of basalt as an

182   analogous. Low concentrations of silica could be increased by adding low cost wastes such as

183   spent foundry sands, which typically contain about 88 wt% of silica (Siddique et al., 2010).

184

185

186

187

188

189

190

191

192

193

Table 1. Chemical composition (wt%) of sewage sludge from wastewater treatment plants in

195   Catalonia and the basalt used as a raw material for the production of glass. The WWTPs are

196   identified by the name of the town they serve.

197

	Centelles	Vic	Taradell	Torelló	Manlleu	Tona	Prats	Roda	St. P. Ribes	Basalt
Al_2O_3	10.40	10.55	11.29	5.35	9.92	11.20	11.35	9.86	13.71	14.37
SiO_2	16.60	17.45	24.19	10.54	19.49	23.59	20.69	18.33	31.6	44.63
CaO	21.25	19.64	14.92	14.34	21.46	22.4	18.85	18.61	30.27	10.26
TiO_2	0.80	0.59	0.75	0.41	0.61	0.96	0.57	0.59	2.00	2.55
Na_2O	1.94	2.19	2.97	1.09	1.27	1.64	1.53	1.85	1.53	3.36
MgO	3.94	3.04	2.35	2.15	2.91	4.85	3.00	3.23	3.36	10.20
MnO	-	0.25	-	-	-	-	-	0.16	0.00	0.17
Fe_2O_3	16.96	21.17	19.97	37.16	18.37	3.03	17.01	20.73	4.32	12.86
K_2O	4.00	1.26	3.00	1.63	2.39	7.22	4.04	2.36	1.80	2.01
P_2O_5	22.29	17.52	19.56	25.64	22.57	23.78	21.15	20.29	7.74	0.56
SO_3	0.92	1.61	0.16	0.37	-	0.38	0.18	0.46	2.86	-
Cr_2O_3	-	3.93	-	0.13	-	-	0.86	2.22	0.00	0.04
NiO	-	-	-	0.13	-	-	0.14	-	0.82	0.02
CuO	0.32	0.28	0.33	0.2	0.15	-	0.27	0.42	0.10	0.01
ZnO	0.18	0.31	0.16	0.63	0.21	0.23	-	0.65	-	0.01
SrO	0.24	0.23	0.16	0.23	0.36	0.58	0.23	0.23	0.12	0.10
BaO	0.17	-	0.18	-	0.29	0.14	0.12	-	0.12	0.07

198

199   3.2. Texture and density: effect of P on the homogeneity of the glasses

200   The nominal compositions of the glasses are shown in Table 2. In the glasses with more than

201   8 wt% P_2O_5 phase separation process – observed by the presence of two phases of different

202   average atomic number in the backscattered electron mode of SEM and TEM (Fig. 1 and Fig. 2)

203   – prevents obtaining consistent experimental bulk chemical compositions. However, the

204   calculations are considered accurate because there is no significant weight loss during melting.

205   The relative concentrations of Al_2O_3, CaO, Na_2O and K_2O correspond to the metaluminous field

206   ([CaO]+[Na_2O]+[K_2O] > [Al_2O_3] > [Na_2O]+[K_2O]).

207

208

209

Table 2. Nominal chemical compositions (wt%) of the major components of the glasses.

wt%/Samples	Basalt	B0	B2P	B4P	B8P	B16P	B32P
Al_2O_3	14.37	14.37	14.08	13.8	13.22	12.07	9.77
SiO_2	44.63	44.63	43.74	42.85	41.06	37.49	30.35
CaO	10.26	10.26	10.06	9.85	9.44	8.62	6.98
TiO_2	2.55	2.55	2.50	2.45	2.35	2.14	1.73
Na_2O	3.36	3.36	3.29	3.23	3.09	2.82	2.29
MgO	10.2	10.20	10.00	9.79	9.38	8.57	6.94
MnO	0.17	0.17	0.17	0.16	0.16	0.14	0.12
FeO	11.88	11.88	11.64	11.41	10.93	9.98	8.08
K_2O	2.01	2.01	1.97	1.93	1.85	1.69	1.37
P_2O_5	0.56	0.56	2.55	4.54	8.52	16.47	32.38

The glasses up to 4 wt% P_2O_5 are homogeneous at the SEM scale (Fig 1). At higher phosphorus contents, a dark light Si-rich phase separates from a bright heavy P-rich phase. At 8 wt% P_2O_5 the onset of this immiscibility can be observed in the form of a Si-rich groundmass where a P-rich liquid phase is segregating in the form of nebula-like clusters (Fig. 1A). Further addition of phosphorus up to 16 wt% P_2O_5 causes the exsolution of larger, rounded P rich regions from the Si - P groundmass (Fig. 1B). In this case, circular Si-rich areas separate inside the P-rich region. At 32 wt% P_2O_5 the groundmass is constituted by a Ca-Mg-Fe phosphate phase, which encloses dark circular Si-rich areas (Fig. 1C). The boundaries between the two regions are sharp. Dendritic stanfieldite ($Ca_4(Mg^{2+}, Fe^{2+}, Mn^{2+})_5(PO_4)_6$) crystals have grown due to the crystallization of the phosphorus-rich region (Fig. 1D). The overall P-rich phase dominates the mix in this case because the bulk amount of P_2O_5 in the glass exceeds that of SiO_2. Fe is associated to P due to the formation of Fe^{3+}-PO_4^{3-} complexes (Ryerson, 1985; Toplis et al., 1994).
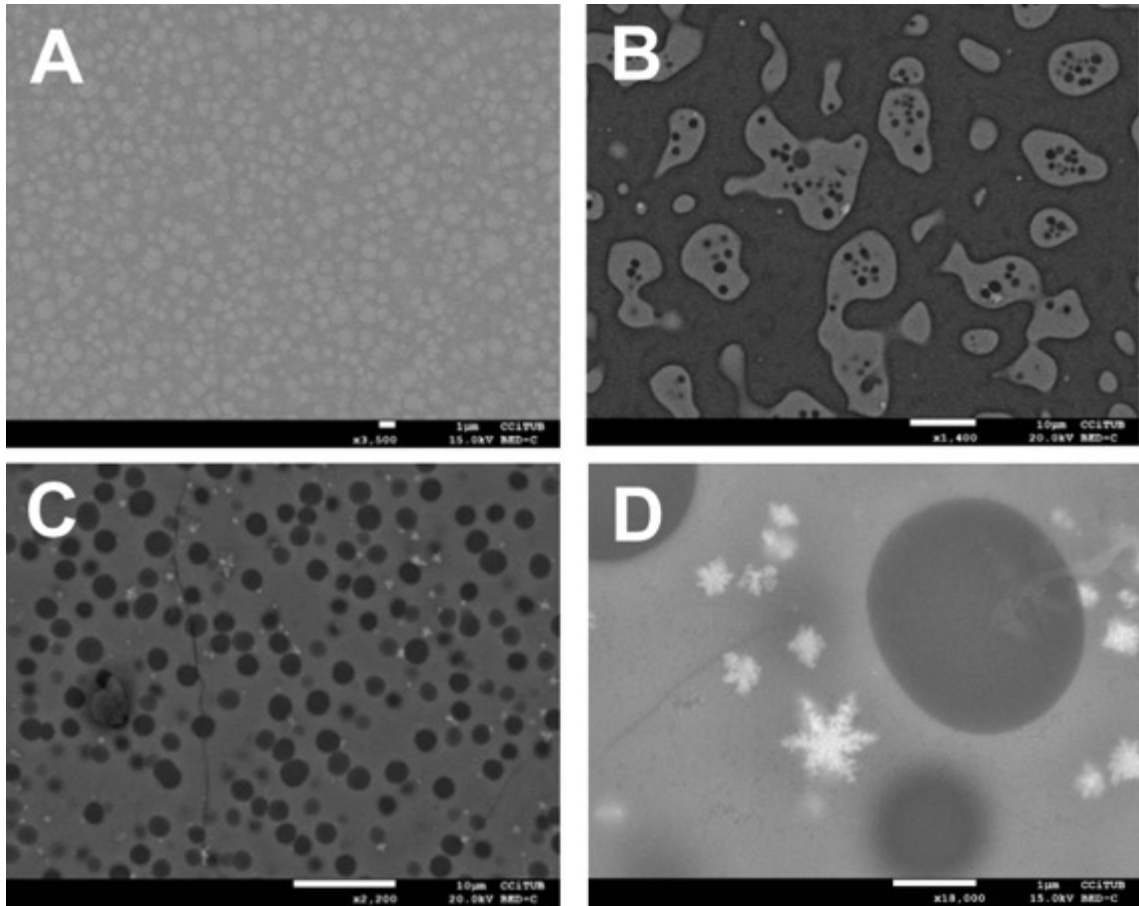
Figure 1. SEM micrographs of the immiscibility of a phosphate-rich and a silicate-rich phases upon phosphorus addition in as-quenched materials. A) Incipient separation in sample B8P. B) The phosphate phase coalesces and the separation with the silicate phase becomes sharper in sample B16P. C) The two phases are in mostly differentiated regions in sample B32P. D). Detail of the sharp separation between the silicate and the phosphate phases.

A characterization of the separation by TEM has provided the chemical compositions of the two unmixed phases in sample B32P. The crystalline phosphate phase has an average of 28.56 mol% P_2O_5. Other major components are MgO (40.02 mol%), CaO (16.39 mol%) and Fe_2O_3 (3.86 mol%). According to these proportions, the limiting component in the crystallization of stoichiometric stanfieldite is CaO. The excess Mg^{2+} and PO_4^{3-} may be forming complexes. The phosphate phase also contains 4.43 mol% Al_2O_3 and 5.13 mol% SiO_2. The silicate phase is mainly constituted by SiO_2 (79.65 mol%) and Al_2O_3 (10.75 mol%), together with 5.31 mol% P_2O_5 and traces of the other components of the basalt. Compositional profiles on the location marked in Fig 2b show a sharp border between the two phases (Fig 2c and d). Moreover, ~~the~~

240 electron diffraction confirms that this phase is amorphous (Fig 2e). The elementary mapping

241 undertaken in a region showing a whole sphere evidences that the aluminosilicate (Fig 2f and g)

242 region is scarce in alkalis and alkaline earths that would act as charge compensators, and which

243 lie mostly in the phosphate phase (Fig. 2 i, j, k, l).

244
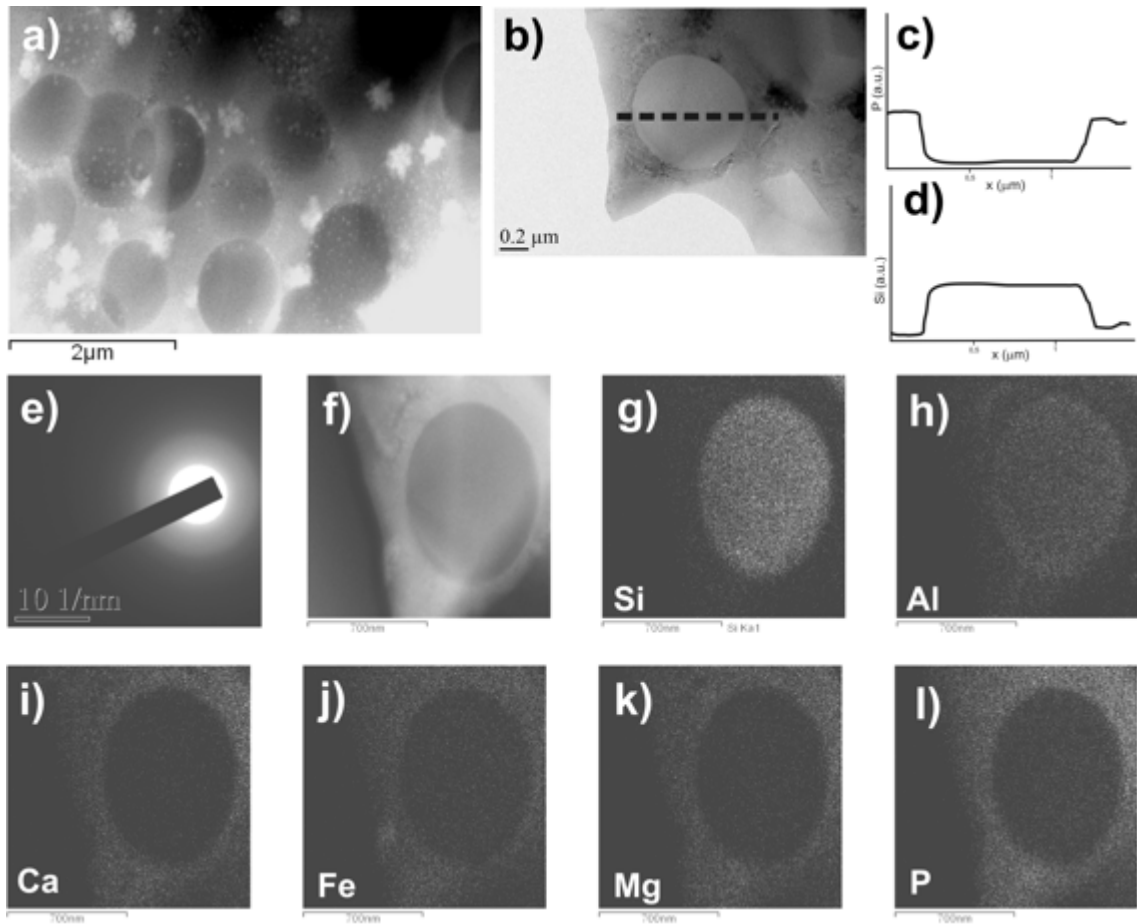
Figure 2. TEM micrographs showing the two unmixed phases in sample B32P (a), elementary composition profiles (b: measured profile, c: P profile; d: Si profile), the electron diffraction profile of the silicate phase (e), location of the mapping (f) and elementary mapping for Si (g), Al (h), Ca (i), Fe (j), Mg (k), P (l).

250 From this point, the materials of this study can be divided in two groups: samples bearing up

251 to 8 wt% P_2O_5 are amorphous at the XRD scale, whereas the unmixed samples have to be

252 considered glass-ceramics.

253 The addition of phosphorus causes a decrease in the average density of the basaltic glass due

254 to the higher free volume of PO_4 tetrahedra compared to SiO_4 tetrahedra (Toplis et al., 1994).

Fig. 3 presents the average densities and the standard deviation of the measurements on 10 different fragments of each composition (vertical error bars). It must be noted that the scatter of the density values shown by the error bars is much larger than the experimental error of ± 0.001 g/cm^3 of the density measurements. Moreover, it increases with P addition, reaching even 0.2 g/cm^3 in sample B32P. This variation of a macroscopic property within a single composition is an indicator of heterogeneities. Thus, the density of the bulk glasses and glass-ceramics actually corresponds to the contribution from the density of nuclei/crystals and the density of the amorphous phase. The higher density values correspond to glass shards enriched in crystalline material. For instance, the highest measured value for sample B32P is 2.95 g/cm^3, close to the actual density of stanfieldite, 3.15 g/cm^3.
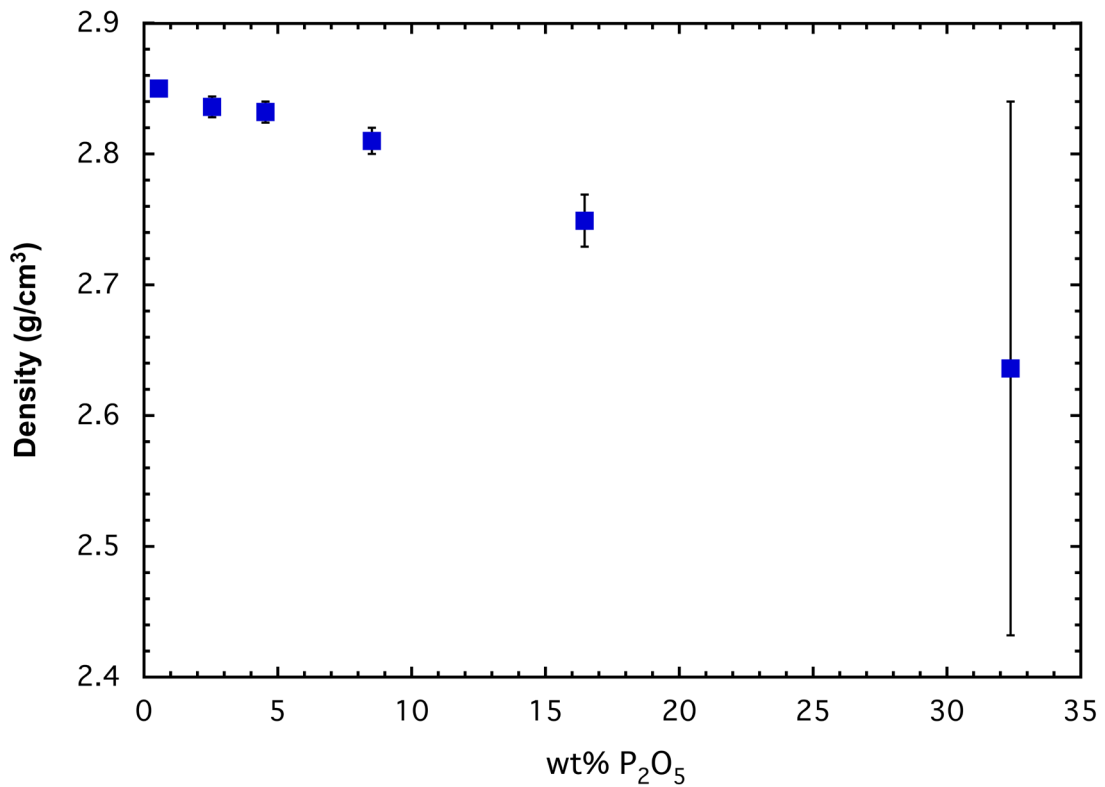
Figure 3. Average densities of the glasses. The error bars show the scatter of the measurements, due to the presence of nanocrystalline domains.

271   3.3. Raman spectroscopy: ordering at the nanoscale

272   Fig. 4 shows the Raman spectra obtained at room temperature of small amounts of glass

273   – some mg at most – molten on the heating wire (Neuville et al., 2014a, 2014b). This melting

274   process achieves faster cooling rates, thus providing a more amorphous material. All samples

275   have been remelted at 1450 ºC (Fig. 4a) and at 1600 ºC (Fig. 4b).

276   Raman spectra of basalts are composed of 3 wide bands: the low frequency envelope (LF)

277   from 200 to 600 cm^{-1}, the middle frequency envelope (MF) from 600 to 800 cm^{-1}, and the high

278   frequency (HF) envelope from 800 to 1200 cm^{-1}. The narrow vibrations that arise from the

279   major bands in the spectra account for the formation of nanocrystalline domains during the

280   supercooling process.

281   In the series molten at 1450 ºC the main band around 673 cm^{-1} at low P contents corresponds

282   to the A_{1g} vibration of magnetite (Shebanova and Lazor, 2003) and it masks the contributions of

283   the LF and MF. These magnetite nanolites are not visible by classic electron microscopy

284   observation because of its very small size. However, Neuville and coworkers identified a mix of

285   magnetite and hercynite with a size of 10·10·5 nm in High Resolution TEM (Neuville et al.,

286   1996). These nanolites might probably be the starting point of the nucleation process. At 8 wt%

287   the bands seem to merge, showing the collapse of the glass structure. The band near 965 cm^{-1} is

288   assigned to the ν_1 mode of crystalline phosphate (Penel et al., 1997); it becomes more intense

289   and shifts to higher frequencies with increasing P. In the series molten at 1600 ºC (Fig. 4b) the

290   main feature is a band arising from the HF envelope at 965 cm^{-1}. As in the former case, it

291   corresponds to a crystalline phosphate (Penel et al., 1997) of a high melting point. For instance,

292   apatite has a melting point between 1608 and 1622 ºC (Bhatnagar, 1969). There is no evidence

293   for the presence of magnetite – the melting point of pure magnetite is 1594 ºC (Deer et al.,

294   1992).

295

296
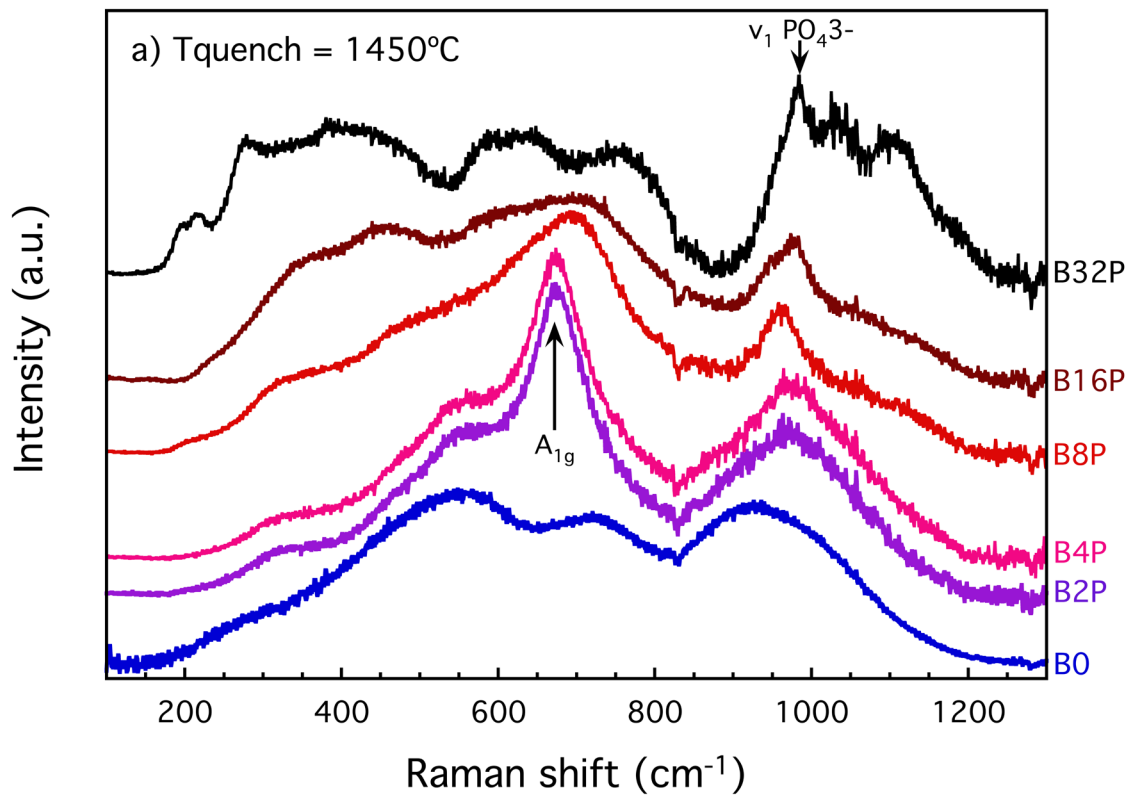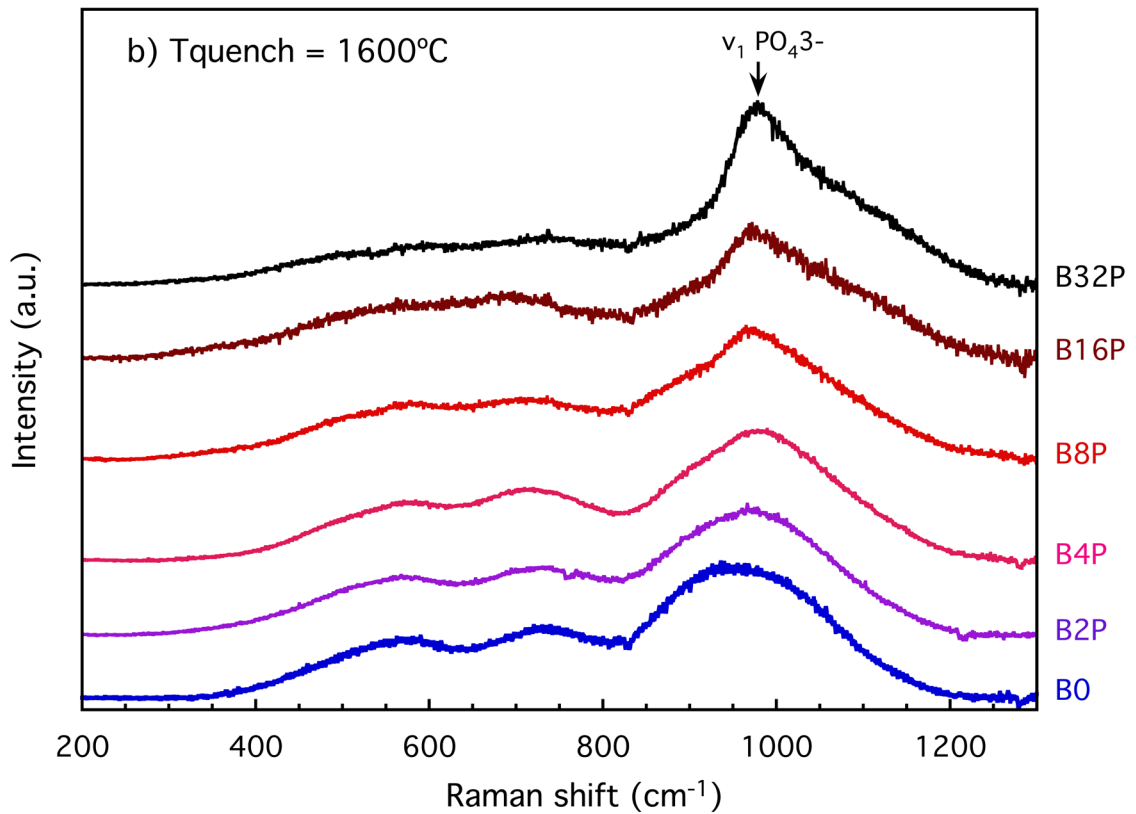
Figure 4. Raman spectra of the glasses remelted at a) 1450 °C and b) 1600 °C on the heating

298   wire.

299

300   The LF envelope is generally assigned to vibrations of the bridging oxygens (BO) forming

301   rings of three or more Si^{4+} tetrahedra (Bell et al., 1968; McMillan and Piriou, 1982; Mysen,

302   2003; Mysen et al., 1980; Neuville et al., 2014a; Neuville and Mysen, 1996; Pasquarello and

303   Car, 1998; Seifert et al., 1982; Umari et al., 2003). A band below 800 cm^{-1} generally dominates

304   the MF region and is attributed to the inter-tetrahedral bending mode of polymerized species. Its

305   intensity decreases with decreasing silica content (Matson et al., 1983; McMillan, 1984; Mysen

306   and Toplis, 2007). The HF envelope contains the vibrations corresponding to the T-O$^-$ bonds –

307   T represents fourfold coordinated cations (mainly Si^{4+}, Al^{3+}, Fe^{3+} and P^{5+}) and O$^-$ are the non-

308   bridging oxygen – and the structural effect of the network-modifying or charge balancing

309   cations (Bell and Dean, 1972; Cicconi et al., 2016, 2015; Cochain et al., 2012; Furukawa et al.,

310   2011; Hehlen and Neuville, 2015; Magnien et al., 2008, 2006; McMillan, 1984; Mysen, 2003;

311   Neuville et al., 2014a). The LF asymmetric envelope is centered around 550 cm^{-1} and overlaps

312   the MF region.

313

314   3.4. Thermal analysis and crystallization

315   The evolution of the thermal behavior and crystallization of the synthetic samples has been

316   studied with a combination of DTA (Fig. 5) and XRD (Fig. 6). The DTA runs of the samples

317   with low P contents show an exothermal event about 850 °C that shifts to higher temperatures

318   with increasing P (Fig. 5). In the basalt glass (B0) the event is assigned to the crystallization of

319   pyroxene and titano-magnetite ($Fe_{3-x}Ti_xO_4$). The addition of phosphorus destabilizes the

320   pyroxene; rhönite ($Ca_2(Mg^{2+}\ Fe^{2+}\ Fe^{3+}\ Ti^{2+})_6(Si,Al)_6O_{20}$), a 4-chained inosilicate, is formed

321   instead (Fig. 6). Rhönite is considered a scarce mineral in magmatic rocks, although it is usually

322   present in undersaturated alkali basalt. A common phase association in rocks of similar

323   composition includes Ti-augite, olivine, nepheline, plagioclase, titanomagnetite and Ti-Ca-

324   amphibole (Kunzmann, 1999). P preferentially stays in the amorphous phase at this stage. The

325   formation of inosilicates and spinel-like phases such as titano-magnetite is interesting because

326   they can host potentially toxic elements such as Zn, Cr, etc.

327

Further addition of $P \geq 8$ wt% P_2O_5 changes the behavior of the melt as the phase separation starts. The main event corresponds to the crystallization of phosphate phase stanfieldite $Ca_4(Mg,Fe^{2+},Mn)_5(PO_4)_6$, that must form from the amorphous phosphate phase . Sample B16P lacks an evident exothermal event; the mineral content is limited to the stanfieldite formed during production. Sample B32P undergoes an exothermal event at 688 ºC corresponding to the crystallization of tridymite in the silicate phase. The virtual lack of crystallization of the last samples is consistent with the formation of a glass-ceramic during quenching.
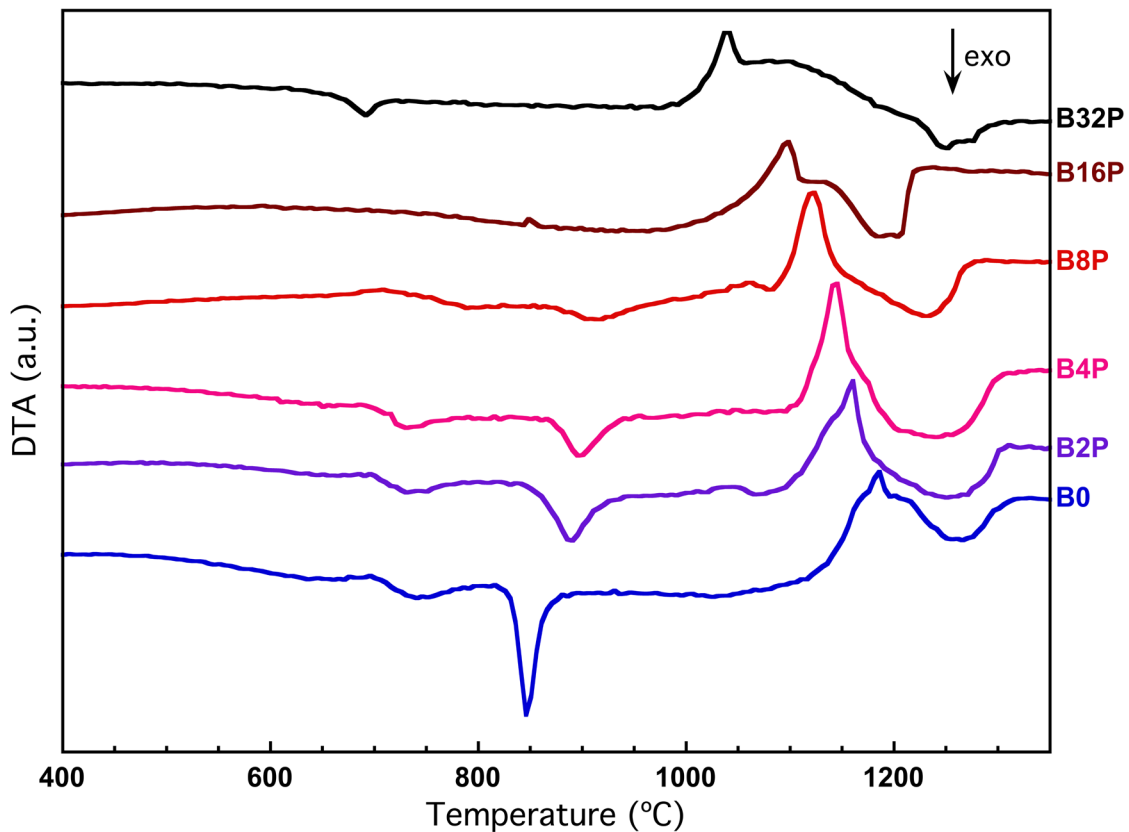
Figure 5. Evolution of the thermal behavior as a function of P contents. The experiments have been performed at a heating rate of 10 ºC/min.

The temperatures of the endothermal events linked to the melting of the system decrease around 170 ºC – from 1200 ºC in the glass of original basalt composition to 1031 ºC in the glass bearing the highest phosphorus concentration (Fig. 5). The depression of liquidus temperature due to the presence of P in silicate systems has previously been reported in albitic and granitic melts, whose liquidus temperatures drop several degrees with P_2O_5 addition. For instance, the

344   melting temperature of albite + 6 wt% P_2O_5 is 150ºC lower than that of the original albite

345   (Wyllie and Tuttle, 1964). The phase diagrams of the pure $Ca_3(PO_4)_2$ - $Mg_3(PO_4)_2$ system show

346   the eutectic melting of the stanfieldite composition at 1120ºC (Ando, 1958). Measured melting

347   temperature is lower due to the higher number of components in the system, which causes

348   impurities to enter the stanfieldite structure.
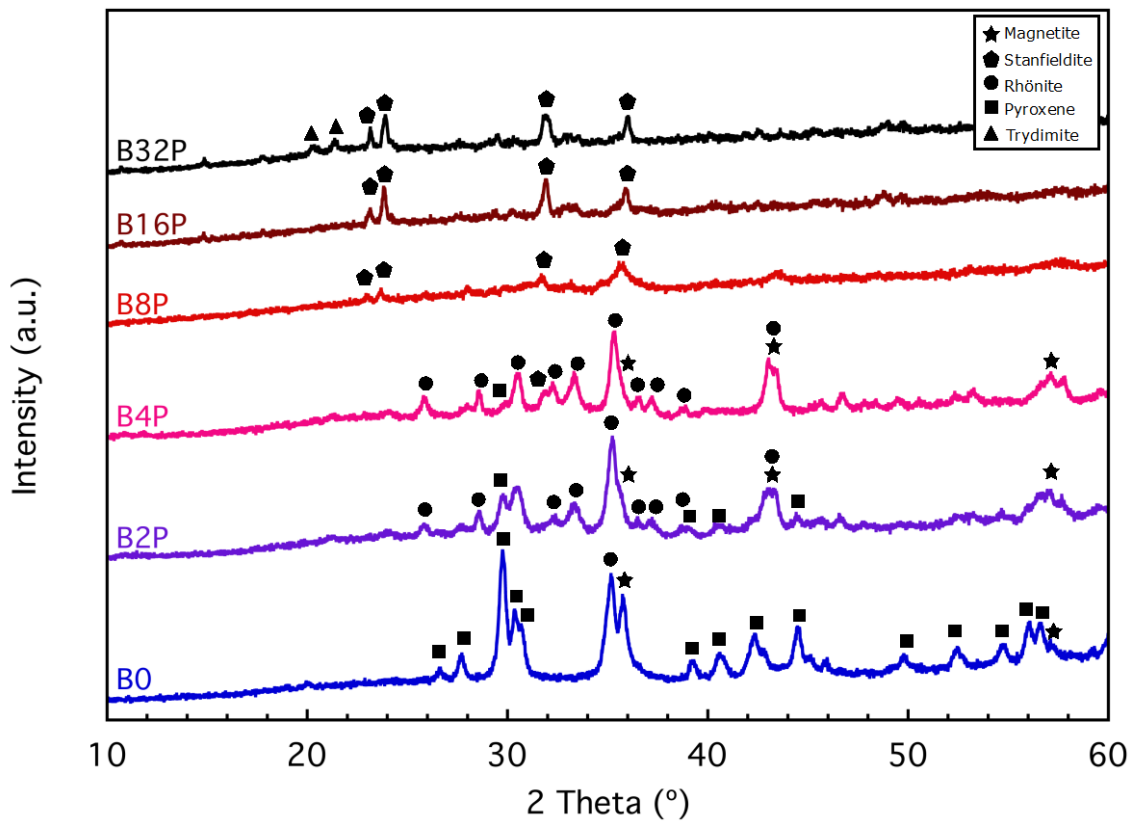
349

350   **Figure 6.** XRD patterns of the thermally treated glasses.

351

352   The mineral association constituted by pyroxene and magnetite has been described in studies

353   about the crystallization of natural melts of basaltic composition (Burkhard, 2001; De Vicente

354   Mingarro et al., 1991). The maximum concentration of P in magmas is around 2 – 3 wt% P_2O_5

355   (Mysen et al., 1999), hence, much lower than the maximum of 32 wt% considered in this study.

356   Increasing P changes the thermal behavior due to the increasing crystallization upon

357   glassmaking. The conditions leading to stability of stanfieldite destabilize the rest of mineral

358   phases: at high P contents, Ca and Mg previously emplaced in the pyroxene structure move to

359   the stanfieldite structure. Fe is also influenced by P both because Fe^{2+} can replace Mg^{2+} in the

360 stanfieldite structure and because of the formation of Fe^{3+}-PO_4^{3-} complexes in the melt. This

361 process also inhibits the crystallization of magnetite, which is consistent with the structural

362 collapse observed on the Raman spectrum of sample B8P quenched at 1450 ºC (Fig. 3a).

363

364 3.5. Rheological behavior and production process

365 Determining viscosity is essential in establishing the temperatures required for industrial

366 glassmaking and processing. Table 3 summarizes the glass transition temperatures (T_g), the

367 temperatures of the fixed viscosity points and the calculated temperatures corresponding to the

368 viscosities of the workability points (annealing, forming, conditioning and melting ranges)

369 (Fernandez Navarro, 1991). T_g values are around 640ºC.

370

371 **Table 3**. Glass transition temperature, measured temperatures corresponding to HSM fixed
372 viscosity points (according to Pascual et al 2001) and calculated temperatures
373 corresponding to viscosities which are significant for glass production.

Viscosity/Pa s	B0	B2P	B4P	B8P	B16P	B32P
T_g / 10^{12}	629	637	639	643	643	650
First shrinkage / $10^{7.9}$	766	799	773	790	943	966
Maximum shrinkage / $10^{6.9}$	946	916	960	880	980	1069
Softening / $10^{5.6}$	1158	1048	1171	1049	1127	1200
Half ball / $10^{3.5}$	1220	1205	1284	1172	1219	1292
Flow / $10^{2.1}$	1254	1305	1317	1238	1276	1323
Annealing range / $10^{13.5-12}$	579-629	578-637	590-639	589-643	570-643	534-650
Forming range / 10^{8-3}	763-1232	795-1241	769-1296	786-1196	838-1239	958-1303
Glass conditioning range / 10^{3-2}	1232-1281	1241-1384	1296-1343	1196-1290	1239-1321	1303-1347

374

375 Viscosities have been plotted as a function of the inverse of temperature (10000/T) of the

376 fixed viscosity points of HSM and compared to viscosity measurements on remelted basalt from

377 Piton de la Fournaise (GBa98) (Villeneuve et al., 2008) (Fig. 7). The plots show an anomalous

378 step in the decrease of viscosity during heating, especially remarkable below 10^8 Pa·s. The

379 cause of the deviation is the growth of nuclei formed during glass production detected by

380 Raman spectroscopy in melts quenched at 1450 ºC. These nuclei cause apparent viscosity to be

381 higher than the actual viscosity of a crystal-free melt of the same composition due to the

382 formation of a biphasic system. At the lower limit of the HSM experiments, the viscosity of the

383   P-doped glasses is similar to that of the remelted natural basalt but at the upper limit –

384   corresponding to the temperature of the flow point; the highest value being 1323ºC for sample

385   B32P – the viscosity is significantly higher than that of the remelted basalt used for comparison.
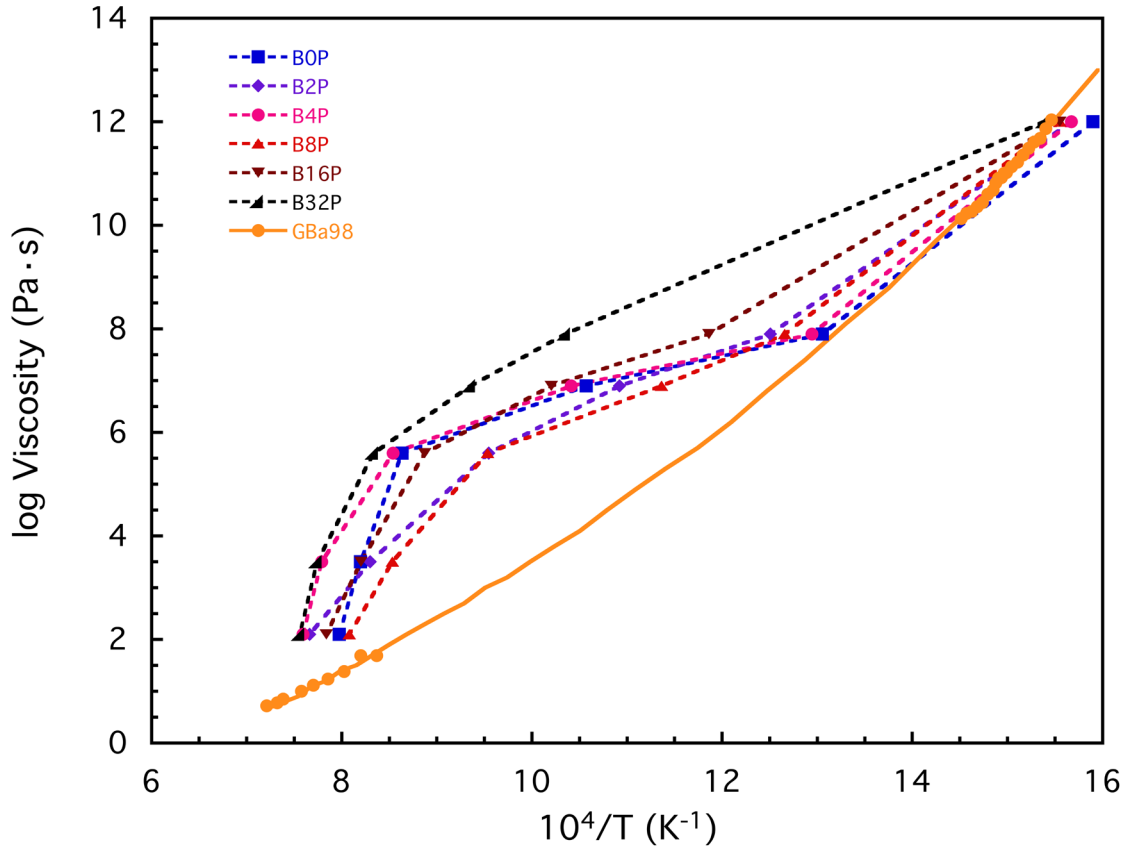
386

387   **Figure 7.** Plot of the viscosity as a function of the inverse of the temperatures of the fixed

388   viscosity points of the glasses and viscosity-temperature curve of a remelted basalt

389   (Villeneuve et al., 2008). Discontinuous lines are only intended as a guide for the eye.

390

391   The variations of viscosity as a function of phosphorus content are influenced by the phases

392   that crystallize during the heating process and by the progress of the immiscibility. In samples

393   from B0 to B4P, when phosphorus contents increase, the onset and the peak of the exothermic

394   (Fig. 5) events shift to higher temperatures due to a delay in crystallization and the increase of

395   apparent viscosity. However, this is in conflict with the increasing degree of crystallinity due to

396   further P addition, which increases viscosity again. The phase separation is another major

397   controller of the evolution of viscosity: in composition B8P the phosphate phase plays the role

of a low viscosity liquid where the silicate regions are immersed. The apparent viscosity in compositions B16P and B32P rises again when both the immiscibility and the crystallinity of the phosphate phase increase.

At low concentrations and in depolymerized melts, phosphorus has been reported to cause a non-linear variation of viscosity. This is attributed to the competition between the depolymerizing effect due to the oxidation of Fe^{2+} – viscosity is decreased – and the polymerizing effect related to the removal of network-modifying cations and formation of Si-O-Si bonds creating highly polymerized regions caused by the addition of P – viscosity is increased (Toplis et al., 1994). This behavior is absent in iron-free compositions; hence it must be attributed to the presence of Fe (Toplis and Dingwell, 1996). P also behaves differently in acidic than in basic melts. Viscosity has an Arrhenian decrease in P-doped haplogranitic melts with increasing P_2O_5 (Dingwell et al., 1993). This increase in viscosity may be attributed to copolymerization of P^{5+} in the silicate network rather than behaving as a network modifier (Ryerson and Hess, 1980). Another point is that the dependence of structural deformation on temperature seems to decrease with increased crystallization caused by P addition.

The melting temperatures during production have to be over the flow point (in this case between 1357 – 1411ºC). According to these results, a production temperature of 1450ºC would be appropriate to cover all the compositional range up to 4 wt% P_2O_5.

3.6. Microhardness

The possibility of using the new materials in the building industry will finally depends on their mechanical properties. The average microhardness of the P-doped basaltic glasses decreases with phosphorus addition from 7.7 GPa in the basaltic glass to 5.4 GPa in sample B32P (Fig. 8). These values are similar to the range of 5.16 – 6.28 GPa reported by Mingarro (De Vicente Mingarro et al., 1991) and 7.7 GPa obtained by Jensen and coworkers (Jensen et al., 2009) for basaltic glasses. All these measurements lie in the range of the majority of conventional glasses and glass-ceramics (Evans and Wilshaw, 1976; Rincón and Capel, 1985). When analyzed in detail, the decrease of microhardness follows two different trends (Figure 8).

426 It has a steep slope until the immiscibility begins; the gradient then becomes much smaller. This

427 is consistent with the formation of a glass-ceramic during the quenching process. The formation

428 of a crystalline phosphate improves the resistance of the final product. The decrease of hardness

429 with P addition can be attributed to the inferior resistance of phosphate materials in comparison

430 to silicates. The most common phosphate mineral, apatite, has a hardness around 5.2 GPa and

431 stanfieldite ranges between 2.0 and 5.2 GPa. On the other hand, the hardness of silicate minerals

432 such as quartz is much higher, between 10.82 and 12.36 GPa.
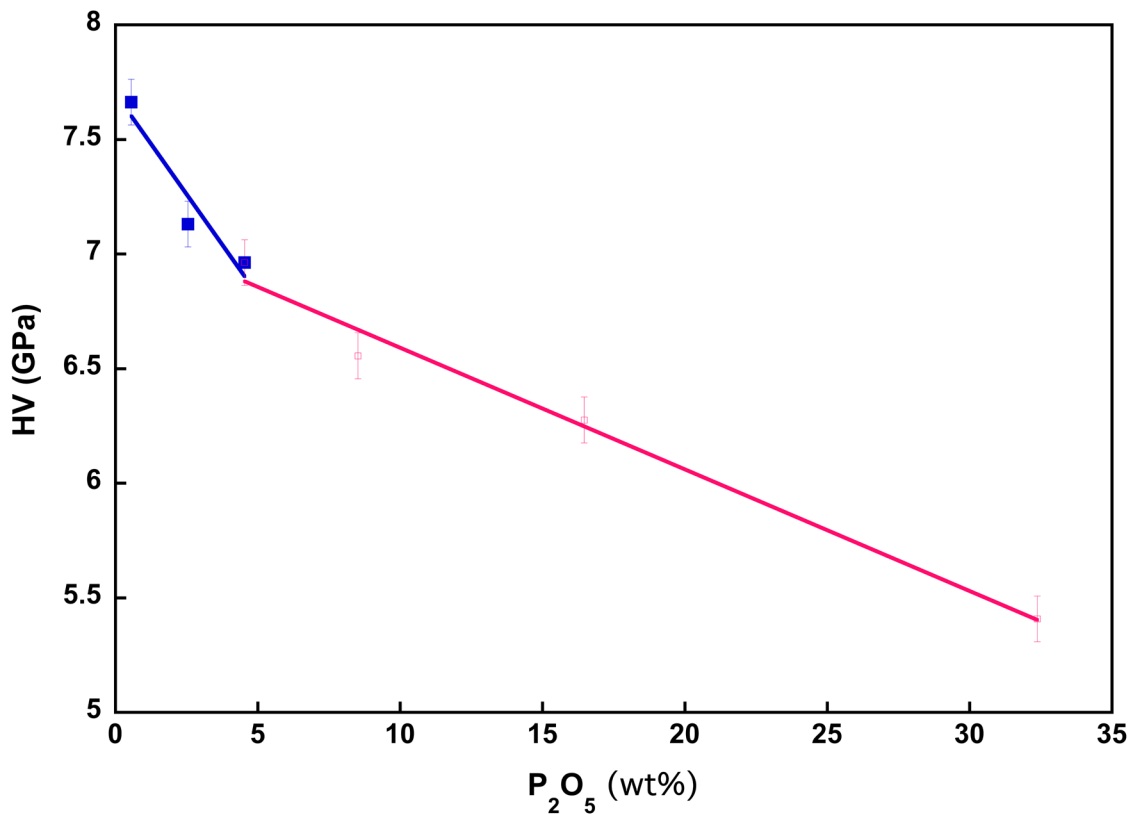
433

434 **Figure 8.** Microhardness (Vickers) of the obtained materials as a function of P contents. The

435 change of the slope between the two fitted lines is due to the diminution in the decrease of

436 microhardness caused by crystallization.

437

438 3.7. Chemical stability

439 The low chemical resistance of phosphate glasses has long been reported in the literature

440 (Brow, 2000; Kreidl and Weyl, 1941), hence creating the necessity to verify that it does not

441 increase the solubility of the basaltic glasses – as it is intended to use them as an inertization

442 matrix. The elementary concentrations in the leachate of the major elements are generally lower

443 than in the deionized water used as a blank (Table 4). Even Si and P, the two major elements,

444 only leach some ppm's, accounting for the stability of the material. Considering the potentially

445 toxic elements, the obtained glasses comply with the limits established in norm DIN 38414-S4

446 for them to be considered inert. Crystalline phosphate phases such as stanfieldite are considered

447 stable in the long term in terrestrial soils (Qian and Jiang, 2014). However, it has to be noted

448 that the amount of P in the leachate doubles between samples B16P and B32P. The leaching of

449 Mg also follows this trend but neither Ca nor Fe do, thus the the leaching has to be limited to the

450 excess unstable Mg^{2+}-PO_4^{3-} complexes. In exchange, the concentration of Si in the leachate

451 increases from sample B0 to B2P and is then reduced as the immiscibility progresses, hence the

452 silicate phase must be becoming more stable. This might signal the onset of the separation

453 actually happens before it can be distinguished in SEM.

454 **Table 4.** Elementary analysis of the leachates after immersion of glass bits in deionized water.

455 BB stands for "below the blank" and BDL for "below detection limit".

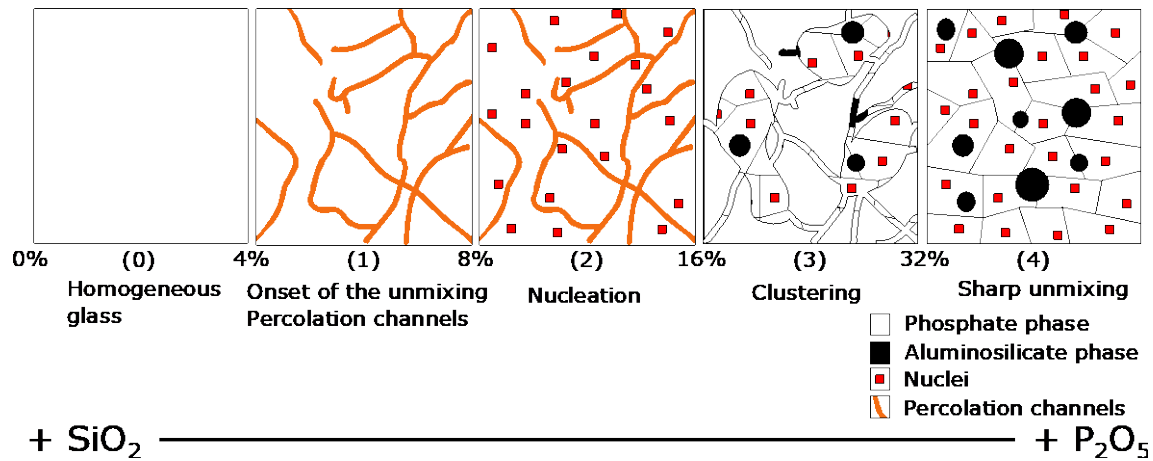| [ppm] in sol	Si	Al	Ca	Mg	Na	K	Fe	P		
B0P	1.71	BDL	BB	0.96	0.20	0.23	BDL	BDL		
B2P	2.47	BDL	BB	1.16	0.38	0.32	BDL	BB		
B4P	2.19	BDL	BB	1.02	0.99	0.34	BDL	BB		
B8P	1.67	BDL	BB	2.22	0.49	0.27	BDL	BB		
B16P	1.28	BDL	BB	2.63	0.00	0.28	BDL	1.88		
B32P	0.35	BDL	BB	3.44	0.06	0.09	BDL	3.83		
[ppb] in sol	As	Ba	Cd	Cr	Cu	Hg	Mn	Ni	Pb	Ti	Zn
B0P	BDL	BB	0.14	BDL	4.03	BDL	BB	BDL	BB	26.14	BB
B2P	BDL	BB	BDL	0.67	BB	BDL	BB	BDL	BB	1.83	BB
B4P	BDL	BB	BDL	BDL	BB	BDL	0.42	BDL	BB	1.90	BB
B8P	BDL	BB	0.00	BDL	3.35	BDL	0.04	BDL	BDL	1.60	BB
B16P	BDL	BB	0.01	BB	BB	BDL	3.63	BDL	BB	4.80	BB
B32P	BDL	BB	BDL	BDL	BB	BDL	5.72	BDL	BB	42.71	BB
DIN38414-S4	500		40	500	2000	100		400	500		4000

456

457

458 **4. Discussion: solubilization of P and immiscibility**

459 It is possible to add large amounts of phosphorus to basaltic glass although it triggers a

460 phase separation. Its development at high P_2O_5 concentrations causes the initially homogeneous

461 glass to evolve into a glass-ceramic. The separation of silicate and phosphate phases can be

462 interpreted in the framework of the Modified Random Network theory (MRN) (Greaves, 1985;

463 Greaves et al., 1981; Le Losq et al., 2017). The MRN model states that in silicate glasses there

464 is a segregation between the network formers (Si^{4+}, Al^{3+} and Fe^{3+}) and the network modifiers

465 (the alkaline and alkaline earth cations) leading to the development of differentiated local

466 structures, called percolation channels, at the nanometer scale (Greaves et al., 1981; Vessal et

467 al., 1992). The formation of percolation channels around silicate tetrahedra is in itself an

468 unmixing process because it separates the aluminosilicate region, rich in network formers (NF),

469 from the network modifiers (NM).

470 The evolution of the system can be summarized in the following steps (Figure 9):

471   -   From 0 to 4 wt% P_2O_5 the glasses are homogeneous (scheme 0). The T_g signal becomes

472   less intense. There is a slight depolymerization related to the diminution of SiO_2 and no

473   gain in polymerization due to the formation of phosphate chains.

474   - $4 <$ wt% $P_2O_5 < 6$ is the beginning of channel formation (scheme 1). Around 6 wt% the

475   nucleation probably starts (scheme 2), hence at 8 wt% P_2O_5 the immiscibility can be

476   observed in SEM although it is still XRD-amorphous. The presence of an amorphous

477   phosphate phase decreases the overall viscosity.

478   - > 8 wt% the combination of immiscibility and nucleation results in increasingly

479   pervasive nanocrystallization and growth in the phosphate phase (scheme 3-4). The

480   formation of a glass-ceramic increases the viscosity of the melt. Crystallization

481   improves microhardness and leachability compared to a scenario where the material

482   stayed in glassy form. For instance, from the extrapolation of the trend of the decrease

483   of microhardness at low P contents (Figure 8), the value of 5.40 GPa at 32 wt% P_2O_5

484   would be reached at 13.08 wt% P_2O_5 if crystallization had not occurred.

0%   (0)   4%   (1)   8%   (2)   16%   (3)   32%   (4)

Homogeneous glass   Onset of the unmixing Percolation channels   Nucleation   Clustering   Sharp unmixing

☐ Phosphate phase
■ Aluminosilicate phase
▪ Nuclei
╲ Percolation channels

485 $+ SiO_2$ ——————————————————————— $+ P_2O_5$

486   Figure 9. Scheme of the incorporation of phosphorus to the glass structure: from a

487   homogeneous glass to a glass-ceramics.

488

489   The bulk compositions of the P-doped glasses and glass-ceramics lie in the

490   metaluminous range $([CaO] + [Na_2O] + [K_2O] > [Al_2O_3] > [Na_2O] + [K_2O])$. P^{5+} can form

491   strong complexes due to its high field strength. Once formed, these complexes reside outside the

492   silicate network. Divalent cations, in this case Ca^{2+}, Mg^{2+}, Fe^{2+} and Mn^{2+}, form stable

493   complexes with P according to reaction (Ryerson and Hess, 1980):

494    $2Mg\text{-}O\text{-}Si + P\text{-}O\text{-}P \leftrightarrows 2Mg\text{-}O\text{-}P + Si\text{-}O\text{-}Si$
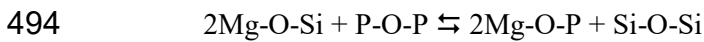
495   This reaction causes a polymerization of the network that enhances the separation of the

496   aluminosilicate spheres (the NF-rich region of the MRN model) and decreases the activities of

497   the NM due to the complexation with P (Gan and Hess, 1992). In the network modifier-rich

498   region, the NM-phosphate groups are more extensive and may be acting as a precursor to the

499   crystallization of stanfieldite that hosts all the main divalent cations in its structure

500    $Ca_4(Mg,Fe^{2+},Mn)_5(PO_4)_6$.

501   The polymerization of the network progresses even further in the aluminosilicate region

502   of sample B32P (around 80 mol% SiO_2, 11 mol% Al_2O_3 and 5 mol% P_2O_5) according to the

503   reaction described by Gan and Hess for the solubilization of P in peraluminous melts of the

504    $Al_2O_3 - SiO_2 - K_2O - P_2O_5$ system:

505    $2Al\text{-}O\text{-}Si + P\text{-}O\text{-}P \leftrightarrows 2Al\text{-}O\text{-}P + Si\text{-}O\text{-}Si$
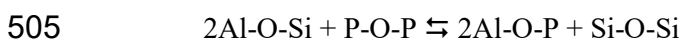
506 where P reacts with excess Al to form $AlPO_4$ species, furthering the polymerization of the
507 silicate network by creating silica-rich clusters (Gan and Hess, 1992). This high polymerization
508 degree enables the spheres to stay amorphous. Although $AlPO_4$ units are electrically neutral,
509 excess Al needs to be charge-balanced as there is a lack of alkali and alkaline-earth elements.
510 This could be achieved by the formation of five- or six-fold coordinated Al (Neuville et al.,
511 2006). An attempt to verify this affirmation by electron energy loss spectroscopy in the TEM
512 equipment has been unsuccessful due to the insufficient concentration of Al.

513 Although it has not been possible to obtain direct evidence of this fact, the boost in
514 viscosity would be consistent with unmixing beginning in the liquid state. The arrangement has
515 to be either very fast to happen during the few seconds that the melt is effectively flowing or
516 already present in the melt, which is consistent with sample B32P having the highest T_g and
517 viscosity. P_2O_5

518

519 **5. Conclusions**

520 Basaltic liquids accept a certain amount of phosphorus, showing potential for the use of
521 sewage sludge as a raw material in the production of glass. The immiscibility between an
522 aluminosilicate and a Ca-Mg-Fe phosphate phase is the limit of single glass formation. After the
523 separation, the phosphate phase will crystallize thus giving glass-ceramics that are capable of
524 hosting and stabilizing large amounts of P.

525 The rheological behavior of the P-doped basaltic melts is controlled by the nucleation
526 of magnetite and stanfieldite during the melting and the quenching processes. Subsequent
527 growth of these nuclei increases the temperatures at which the viscosity of the melt reaches the
528 forming and glass conditioning ranges (viscosities from 10^8 to 10^2 Pa·s).

529 The devitrification caused by thermal treatments is constrained by the liquid-liquid
530 immiscibility. At low P contents the glass will crystallize into magnetite and either pyroxene or
531 rhönite. This association stands out because of the possibility that further inertization could be
532 achieved by means of a glass-ceramic process – due to the ability of inosilicates and spinel-like
533 phases (magnetite) to host potentially toxic elements such as Cr or Ba. At high P contents the

534 separation forces the crystallization of the phosphate rich phase into stanfieldite, whereas the

535 silica rich phase mainly stays amorphous due to both its high Si contents and the lack of

536 nucleating agents such as Fe or Ti.

537   The microhardness of the glasses is comparable to other petrurgic basaltic materials.

538 According to the leaching tests, the glasses can be considered inert because the cations are

539 bound in the structure of the glass especially at low P contents. The inertization of high amounts

540 of phosphorus is possible because crystallization of a phosphate phase/stanfieldite buffers the

541 loss of mechanical and chemical resistance typical of phosphate glasses.

542

550

551 **7. References**

552 Ando, J., 1958. Phase Diagrams of $Ca_3(PO_4)_2$-Mg_3 $(PO_4)_2$ and $Ca_3(PO_4)_2$-$CaNaPO_4$. Bull. Chem.
553   Soc. Jpn. 31, 201–205.

554 Bell, R.J., Bird, N.F., Dean, P., 1968. The vibrational spectra of vitreous silica, germania and
555   beryllium fluoride. J. Phys. C Solid State Phys. 1, 299–303. https://doi.org/10.1088/0022-
556   3719/1/2/304

557 Bell, R.J., Dean, P., 1972. Localization of phonons in vitreous silica and related glasses. Int.
558   Conf. Phys. Non-Crystalline Solids 22, 375–382.

559 Bhatnagar, V.M., 1969. The melting point of synthetic apatites. Mineral. Mag. 37, 288.

560 Binhussain, M.A., Marangoni, M., Bernardo, E., Colombo, P., 2014. Sintered and glazed glass-
561   ceramics from natural and waste raw materials. Ceram. Int. 40, 3543–3551.
562   https://doi.org/10.1016/j.ceramint.2013.09.074

563 Borowski, S., Domański, J., Weatherley, L., 2014. Anaerobic co-digestion of swine and poultry
564   manure with municipal sewage sludge. Waste Manag. 34, 513–521.
565   https://doi.org/10.1016/j.wasman.2013.10.022

566 Brow, R.K., 2000. Review: the structure of simple phosphate glasses. J. Non. Cryst. Solids 263,
567   1–28. https://doi.org/10.1016/S0022-3093(99)00620-1

568 Burkhard, D.J.M., 2001. Crystallization and oxidation of Kilauea basalt glass: Processes during
569   reheating experiments. J. Petrol. 42, 507–527 ST–Crystallization and oxidation of Kil.
570   https://doi.org/10.1093/petrology/42.3.507

Careghini, A., Dastoli, S., Ferrari, G., Saponaro, S., Bonomo, L., De Propris, L., Gabellini, M., 2010. Sequential solidification/stabilization and thermal process under vacuum for the treatment of mercury in sediments. J. Soils Sediments 10, 1646–1656. https://doi.org/10.1007/s11368-010-0290-7

Cheng, T.W., 2004. Effect of additional materials on the properties of glass-ceramic produced from incinerator fly ashes. Chemosphere 56, 127–131. https://doi.org/10.1016/j.chemosphere.2004.02.009

Cheng, T.W., Ueng, T.H., Chen, Y.S., Chiu, J.P., 2002. Production of glass-ceramic from incinerator fly ash. Ceram. Int. 28, 779–783. https://doi.org/10.1016/S0272-8842(02)00043-3

Cicconi, M.R., De Ligny, D., Gallo, T.M., Neuville, D.R., 2016. Ca neighbors from XANES spectroscopy: A tool to investigate structure, redox, and nucleation processes in silicate glasses, melts, and crystals. Am. Mineral. 101. https://doi.org/10.2138/am-2016-5663

Cicconi, M.R., Neuville, D.R., Tannou, I., Baudelet, F., Floury, P., Paris, E., Giuli, G., 2015. Letter. Competition between two redox states in silicate melts: An in-situ experiment at the Fe K-edge and Eu L_3-edge. Am. Mineral. 100, 1013–1016. https://doi.org/10.2138/am-2015-5172

Ciecińska, M., Stoch, P., Stoch, A., Nocuń, M., 2015. Thermal properties of 60P2O5-20Fe2O3-20Al2O3 glass for salt waste immobilization. J. Therm. Anal. Calorim. 121, 1225–1232. https://doi.org/10.1007/s10973-015-4586-0

Cochain, B., Neuville, D.R., Henderson, G.S., McCammon, C.A., Pinet, O., Richet, P., 2012. Effects of the iron content and redox state on the structure of sodium borosilicate glasses: A Raman, Mössbauer and boron K-edge XANES spectroscopy study. J. Am. Ceram. Soc. 95, 962–971. https://doi.org/10.1111/j.1551-2916.2011.05020.x

Correll, D.L., 1998. The Role of Phosphorus in the Eutrophication of Receiving Waters: A Review. J. Environ. Qual. 27, 261. https://doi.org/10.2134/jeq1998.00472425002700020004x

Davydov, V.I., Burdinskii, V.P., Dobrygin, P.G., Luchnikov, N.V., Kostin, V.V., Filippov, S.N., Kolupaeva, T.I., 1996. Equipment for vitrification of nuclear power plant wastes in a direct-heating ceramic furnace. At. Energy 80, 219–221.

De Vicente Mingarro, I., Callejas, P., Rincon, J.M., 1991. Microestructura y microanálisis de fases minerales cristalizadas en vidrios obtenidos a partir de rocas basálticas. Bol. la Soc. Esp. Mineral. 14, 95–105.

Deer, W.A., Howie, R.A., Zussman, J., 1992. An introduction to the rock-forming minerals, 2nd ed. Longman.

DIN-38414S4, 1984. Deutsche Einheitsverfahren zur Wasser, Abwasserund Schlammuntersuchung, Bestimmung der Eluierbarkeit von Wasser (S4).

Dingwell, D.B., Knoche, R., Webb, S.L., 1993. The effect of P_2O_5 on the viscosity of haplogranitic liquid . Eur. J. Miner. 5, 133–140.

Dupree, R., Holland, D., Mortuza, M.G., Collins, J.A., Lockyer, M.W.G., 1989. Magic angle spinning NMR of alkali phospho-alumino-silicate glasses. J. Non. Cryst. Solids 112, 111–119. https://doi.org/10.1016/0022-3093(89)90504-8

European Council, 1986. Directive 86/278/EEC and of the European Council on the protection of the environment, and in particular of soil, when sewage sludge is used in agriculture. Off. J. Eur. Communities. L Ser. L 269, 1–13. https://doi.org/2004R0726 - v.7 of 05.06.2013

Evans, A.G., Wilshaw, T.R., 1976. Quasi-static solid particle damage in brittle solids-I. Observations analysis and implications. Acta Metall. 24, 939–956. https://doi.org/10.1016/0001-6160(76)90042-0

Fernandez Navarro, J.M., 1991. El vidrio. Consejo Superior de Investigaciones Científicas.

Folgueras, M.B., Díaz, R.M., Xiberta, J., Prieto, I., 2003. Thermogravimetric analysis of the co-combustion of coal and sewage sludge. Fuel 82, 2051–2055. https://doi.org/10.1016/S0016-2361(03)00161-3

Forsberg, L.S., Ledin, S., 2006. Effects of sewage sludge on pH and plant availability of metals in oxidising sulphide mine tailings. Sci. Total Environ. 358, 21–35.

626   https://doi.org/10.1016/j.scitotenv.2005.05.038

627 Furukawa, T., Fox, K.E., White, W.B., 2011. intensities and structural units in sodium silicate
628   glasses Raman spectroscopic investigation of the structure of silicate glasses . III . Raman
629   intensities and structural units in sodium silicate glasses 8) 3226.
630   https://doi.org/10.1063/1.442472

631 Gan, H., Hess, P.C., 1992. Phosphate speciation in potassium aluminosilicate glasses. Am.
632   Mineral. 77, 495–506.

633 Garcia-Valles, M., Avila, G., Martinez, S., Terradas, R., Nogues, J.M., 2007. Heavy metal-rich
634   wastes sequester in mineral phases through a glass-ceramic process. Chemosphere 68,
635   1946–1953. https://doi.org/10.1016/j.chemosphere.2007.02.034

636 Garcia-Valles, M., Hafez, H.S., Cruz-Matias, I., Verges, E., Aly, M.H., Nogues, J., Ayala, D.,
637   Martinez, S., 2013. Calculation of viscosity-temperature curves for glass obtained from
638   four wastewater treatment plants in Egypt. J. Therm. Anal. Calorim. 111, 107–114.
639   https://doi.org/10.1007/s10973-012-2232-7

640 Greaves, G.N., 1985. EXAFS and the structure of glass. J. Non. Cryst. Solids 71, 203–217.
641   https://doi.org/10.1016/0022-3093(85)90289-3

642 Greaves, G.N., Fontaine, A., Lagarde, P., D., R., Gurman, S.J., 1981. Local structure of silicate
643   glasses. Nature 293, 611–616. https://doi.org/10.1038/293611a0

644 Haugsten, K.E., Gustavson, B., 2000. Environmental properties of vitrified fly ash from
645   hazardous and municipal waste incineration. Waste Manag. 20, 167–176.
646   https://doi.org/10.1016/S0956-053X(99)00325-6

647 Hehlen, B., Neuville, D.R., 2015. Raman response of network modifier cations in alumino-
648   silicate glasses. J. Phys. Chem. B 119, 4093–4098. https://doi.org/10.1021/jp5116299

649 Hossain, M.K., Strezov, V., Nelson, P.F., 2009. Thermal characterisation of the products of
650   wastewater sludge pyrolysis. J. Anal. Appl. Pyrolysis 85, 442–446.
651   https://doi.org/10.1016/j.jaap.2008.09.010

652 Hrma, P., Riley, B.J., Crum, J. V., Matyas, J., 2014. The effect of high-level waste glass
653   composition on spinel liquidus temperature. J. Non. Cryst. Solids 384, 32–40.
654   https://doi.org/10.1016/j.jnoncrysol.2013.02.014

655 Jensen, M., Smedskjaer, M.M., Estrup, M., Kristjansson, M., Lönnroth, N., Yue, Y.Z., 2009.
656   Hardness of basaltic glass-ceramics. Glas. Technol. Eur. J. Glas. Sci. Technol. Part A 50,
657   189–195.

658 Jung, C.H., Matsuto, T., Tanaka, N., 2005. Behavior of metals in ash melting and gasification-
659   melting of municipal solid waste (MSW). Waste Manag. 25, 301–310.
660   https://doi.org/10.1016/j.wasman.2004.08.012

661 Kavouras, P., Kaimakamis, G., Ioannidis, T.A., Kehagias, T., Komninou, P., Kokkou, S.,
662   Pavlidou, E., Antonopoulos, I., Sofoniou, M., Zouboulis, A., Hadjiantoniou, C.P., Nouet,
663   G., Prakouras, A., Karakostas, T., 2003. Vitrification of lead-rich solid ashes from
664   incineration of hazardous industrial wastes. Waste Manag. 23, 361–371.
665   https://doi.org/10.1016/S0956-053X(02)00153-8

666 Kikuchi, R., 1998. Vitrification process for treatment of sewage sludge and incineration ash. J.
667   Air Waste Manag. Assoc. 48, 1112–1115.
668   https://doi.org/10.1080/10473289.1998.10463766

669 Kreidl, N.J., Weyl, W.A., 1941. Phosphates in Ceramic Ware: Iv, Phosphate Glasses. J. Am.
670   Ceram. Soc. 24, 372–378. https://doi.org/10.1111/j.1151-2916.1941.tb15444.x

671 Kunzmann, T., 1999. The aenigmatite-rhonite mineral group. Eur. J. Mineral. 11, 743–756.

672 Le Losq, C., Neuville, D.R., Chen, W., Florian, P., Massiot, D., Zhou, Z., Greaves, G.N., 2017.
673   Percolation channels: a universal idea to describe the atomic structure and dynamics of
674   glasses and melts. Sci. Rep. 7, 16490. https://doi.org/10.1038/s41598-017-16741-3

675 Long, D.A., 1977. Raman spectroscopy. McGraw-Hill.

676 Magnien, V., Neuville, D.R., Cormier, L., Roux, J., Hazemann, J.L., de Ligny, D., Pascarelli, S.,
677   Vickridge, I., Pinet, O., Richet, P., 2008. Kinetics and mechanisms of iron redox reactions
678   in silicate melts: The effects of temperature and alkali cations. Geochim. Cosmochim.
679   Acta 72, 2157–2168. https://doi.org/10.1016/j.gca.2008.02.007

680 Magnien, V., Neuville, D.R., Cormier, L., Roux, J., Hazemann, J.L., Pinet, O., Richet, P., 2006.

Kinetics of iron redox reactions in silicate liquids: A high-temperature X-ray absorption and Raman spectroscopy study. J. Nucl. Mater. 352, 190–195. https://doi.org/10.1016/j.jnucmat.2006.02.053

Marinoni, N., D'Alessio, D., Diella, V., Pavese, A., Francescon, F., 2013. Effects of soda-lime-silica waste glass on mullite formation kinetics and micro-structures development in vitreous ceramics. J. Environ. Manage. 124, 100–107. https://doi.org/10.1016/j.jenvman.2013.02.048

Matson, D.W., Sharma, S.K., Philpotts, J.A., 1983. The structure of high-silica alkali-silicate glasses. A Raman spectroscopic investigation. J. Non. Cryst. Solids 58, 323–352. https://doi.org/10.1016/0022-3093(83)90032-7

McMillan, P., Piriou, B., 1982. The structures and vibrational spectra of crystals and glasses in the silica-alumina system. J. Non. Cryst. Solids 53, 279–298. https://doi.org/10.1016/0022-3093(82)90086-2

McMillan, P.F., 1984. Structural Studies of Silicate Glasses and Melts-Applications and Limitations of Raman Spectroscopy. Am. Mineral. 69, 622–644. https://doi.org/0003-004x/84/070E-0622$0

Mininni, G., Blanch, A.R., Lucena, F., Berselli, S., 2015. EU policy on sewage sludge utilization and perspectives on new approaches of sludge management. Environ. Sci. Pollut. Res. 22, 7361–7374. https://doi.org/10.1007/s11356-014-3132-0

Montero, M.A., Jordán, M.M., Hernández-Crespo, M.S., Sanfeliu, T., 2009. The use of sewage sludge and marble residues in the manufacture of ceramic tile bodies. Appl. Clay Sci. 46, 404–408. https://doi.org/10.1016/j.clay.2009.10.013

Mymrin, V., Ribeiro, R.A.C., Alekseev, K., Zelinskaya, E., Tolmacheva, N., Catai, R., 2014. Environment friendly ceramics from hazardous industrial wastes. Ceram. Int. 40, 9427–9437. https://doi.org/10.1016/j.ceramint.2014.02.014

Mysen, B.O., 2003. Physics and chemistry of silicate glasses and melts. Eur. J. Mineral. 15, 781–802.

Mysen, B.O., Frantz, J.D., 1992. Raman spectroscopy of silicate melts at magmatic temperatures: Na_2O-SiO_2 , K_2O-SiO_2 and Li_2O-SiO_2 binary compositions in the temperature range 25-1475° C. Chem. Geol. 96, 321–332. https://doi.org/10.1016/0009-2541(92)90062-A

Mysen, B.O., Holtz, F., Pichavant, M., Beny, J.M., Montel, J.M., 1999. The effect of temperature and bulk composition on the solution mechanism of phosphorus in peraluminous haplogranitic magma. Am. Mineral. 84, 1336–1345. https://doi.org/10.2138/am-1999-0910

Mysen, B.O., Ryerson, F.J., Virgo, D., 1981. The structural role of phosphorus in silicate melts. Am. Mineral. 66, 106–117. https://doi.org/0003-w4x/ 8 | /0 1 02-0 I 06$02.00

Mysen, B.O., Toplis, M.J., 2007. Structural behavior of Al^{3+} in peralkaline, metaluminous, and peraluminous silicate melts and glasses at ambient pressure. Am. Mineral. 92, 933–946. https://doi.org/10.2138/am.2007.2334

Mysen, B.O., Virgo, D., Harrison, W.J., Scarfe, C.M., 1980. Solubility mechanisms of H_2O in silicate melts at high pressures and temperatures: a Raman spectroscopic study: discussion. Am. Mineral. 65, 900–914.

Navarro, A., Cardellach, E., Cañadas, I., Rodríguez, J., 2013. Solar thermal vitrification of mining contaminated soils. Int. J. Miner. Process. 119, 65–74. https://doi.org/10.1016/j.minpro.2012.12.002

Neuville, D.R., Cormier, L., Massiot, D., 2006. Al coordination and speciation in calcium aluminosilicate glasses: Effects of composition determined by ^{27}Al MQ-MAS NMR and Raman spectroscopy. Chem. Geol. 229, 173–185. https://doi.org/10.1016/j.chemgeo.2006.01.019

Neuville, D.R., de Ligny, D., Henderson, G.S., 2014a. Advances in Raman Spectroscopy Applied to Earth and Material Sciences. Rev. Mineral. Geochemistry 78, 509–541. https://doi.org/10.2138/rmg.2013.78.13

Neuville, D.R., Hennet, L., Florian, P., de Ligny, D., 2014b. In situ High-Temperature Experiments. Rev. Mineral. Geochemistry 78. https://doi.org/10.2138/rmg.2013.78.19

736   Neuville, D.R., Linard, Y., Richet, P., 1996. Rheology of iron aluminosilicate melts. Eos
737   (Washington. DC). 77, F798.
738   Neuville, D.R., Mysen, B.O., 1996. Role of aluminium in the silicate network: In situ, high-
739   temperature study of glasses and melts on the join SiO_2-$NaAlO_2$. Geochim. Cosmochim.
740   Acta 60, 1727–1737. https://doi.org/10.1016/0016-7037(96)00049-X
741   Pascual, M.J., Pascual, L., Duran, A., 2001. Determination of the viscosity-temperature curve
742   for glasses on the basis of the fixed viscosity points determined by hot stage microscopy.
743   Phys. Chem. Glas. 42, 61–66.
744   Pasquarello, A., Car, R., 1998. Identification of Raman Defect Lines as Signatures of Ring
745   Structures in Vitreous Silica. Phys. Rev. Lett. 80, 5145–5147.
746   https://doi.org/10.1103/PhysRevLett.80.5145
747   Penel, G., Leroy, G., Rey, C., Sombret, B., Huvenne, J.P., Bres, E., 1997. Infrared and Raman
748   microspectrometry study of fluor-fluor-hydroxy and hydroxy-apatite powders. J. Mater.
749   Sci. Mater. Med. 8, 271–276. https://doi.org/10.1023/A:1018504126866
750   Pioro, L.S., Sadovskiy, B.F., Pioro, I.L., 2001. Research and development of a high-efficiency
751   one-stage melting converter-burial-bunker method for vitrification of high-level
752   radioactive wastes. Nucl. Eng. Des. 205, 133–144. https://doi.org/10.1016/S0029-
753   5493(00)00349-6
754   Qian, T., Jiang, H., 2014. Migration of Phosphorus in Sewage Sludge during Different Thermal
755   Treatment Processes. Sustain. Chem. Eng. 2, 1411–1419.
756   Rincon, J.M., 2016. Vitreous and ceramic processing for the recycling of industrial wastes. Key
757   Eng. Mater. 663, 11–22.
758   Rincón, J.M., Capel, F., 1985. Microindentation behaviour KIC factor determination and
759   microstructure analyses of some Li_2O-SiO_2 glass-ceramic materials. Ceram. Int. 11, 97–
760   102.
761   Roig, N., Sierra, J., Martí, E., Nadal, M., Schuhmacher, M., Domingo, J.L., 2012. Long-term
762   amendment of Spanish soils with sewage sludge: Effects on soil functioning. Agric.
763   Ecosyst. Environ. 158, 41–48. https://doi.org/10.1016/j.agee.2012.05.016
764   Romero, M., Rincón, J.M., 1997. Microstructural characterization of a goethite waste from zinc
765   hydrometallurgical process. Mater. Lett. 31, 67–73. https://doi.org/10.1016/S0167-
766   577X(96)00235-2
767   Romero, M., Rincón, J.M., Rawlings, R.D., Boccaccini, A.R., 2001. Use of vitrified urban
768   incinerator waste as raw material for production of sintered glass-ceramics. Mater. Res.
769   Bull. 36, 383–395. https://doi.org/10.1016/S0025-5408(01)00501-3
770   Ryerson, F.J., 1985. Oxide solution mechanisms in silicate melts: Systematic variations in the
771   activity coefficient of SiO_2. Geochim. Cosmochim. Acta 49, 637–649.
772   https://doi.org/10.1016/0016-7037(85)90159-0
773   Ryerson, F.J., Hess, P.C., 1980. The role of P_2O_5 in silicate melts. Geochim. Cosmochim. Acta
774   44, 611–624. https://doi.org/10.1016/0016-7037(80)90253-7
775   Ryerson, F.J., Hess, P.C., 1978. Implications of liquid-liquid distribution coefficients to
776   mineral-liquid partitioning. Geochim. Cosmochim. Acta 42, 921–932.
777   https://doi.org/10.1016/0016-7037(78)90103-5
778   Seifert, F.A., Mysen, B.O., Virgo, D., 1982. Three-dimensional network structure of quenched
779   melts (glass) in the systems SiO_2-$NaAlO_2$, SiO_2-$CaAl_2O_4$and SiO_2-$MgAl_2O_4$. Am. Mineral.
780   67, 696–717.
781   Shebanova, O.N., Lazor, P., 2003. Raman study of magnetite (Fe_3O_4): Laser-induced thermal
782   effects and oxidation. J. Raman Spectrosc. 34, 845–852. https://doi.org/10.1002/jrs.1056
783   Siddique, R., Kaur, G., Rajor, A., 2010. Waste foundry sand and its leachate characteristics.
784   Resour. Conserv. Recycl. 54, 1027–1036. https://doi.org/10.1016/j.resconrec.2010.04.006
785   Teixeira, S.R., Magalhães, R.S., Arenales, A., Souza, A.E., Romero, M., Rincón, J.M., 2014.
786   Valorization of sugarcane bagasse ash: Producing glass-ceramic materials. J. Environ.
787   Manage. 134, 15–19. https://doi.org/10.1016/j.jenvman.2013.12.029
788   Toplis, M.J., Dingwell, D.B., 1996. The variable influence of P_2O_5 on the viscosity of melts of
789   differing alkali/aluminium ratio: Implications for the structural role of phosphorus in
790   silicate melts. Geochim. Cosmochim. Acta 60, 4107–4121. https://doi.org/10.1016/S0016-

791   7037(96)00225-6

792 Toplis, M.J., Dingwell, D.B., Libourel, G., 1994. The effect of phosphorus on the iron redox
793   ratio, viscosity, and density of an evolved ferro-basalt. Contrib. to Mineral. Petrol. 117,
794   293–304. https://doi.org/10.1007/BF00310870

795 Umari, P., Gonze, X., Pasquarello, A., 2003. Concentration of Small Ring Structures in Vitreous
796   Silica from a First-Principles Analysis of the Raman Spectrum. Phys. Rev. Lett. 90, 4.
797   https://doi.org/10.1103/PhysRevLett.90.027401

798 Varitis, S., Pavlidou, E., Kavouras, P., Vourlias, G., Chrissafis, K., Xenidis, a., Karakostas, T.,
799   2015. Devitrification routes of a vitrified chromium-loaded ash. J. Therm. Anal. Calorim.
800   121, 203–208. https://doi.org/10.1007/s10973-015-4539-7

801 Vessal, B., Greaves, G.N., Marten, P.T., Chadwick, A. V, Mole, R., Houde-Walter, S., 1992.
802   Cation microsegregation and ionic mobility in mixed alkali glasses. Nature 356, 504–506.
803   https://doi.org/10.1038/356504a0

804 Villeneuve, N., Neuville, D.R., Boivin, P., Bachèlery, P., Richet, P., 2008. Magma
805   crystallization and viscosity: A study of molten basalts from the Piton de la Fournaise
806   volcano (La Réunion island). Chem. Geol. 256, 241–250.
807   https://doi.org/10.1016/j.chemgeo.2008.06.039

808 Wang, X., Jin, Y., Wang, Z., Mahar, R.B., Nie, Y., 2008. A research on sintering characteristics
809   and mechanisms of dried sewage sludge. J. Hazard. Mater. 160, 489–494.
810   https://doi.org/10.1016/j.jhazmat.2008.03.054

811 Werner, W., 2012. Section 6. Fertilizers, in: Ulhmann's Encyclopedia of Chemistry. pp. 295–
812   311.

813 Wyllie, P.J., Tuttle, O.F., 1964. Experimental investigation of silicate systems containing two
814   volatile components. Part III. The effects of SO_3, P_2O_5, HCl, and Li_2O, in addition to H_2O,
815   on the melting temperatures of albite and gran. Am. J. Sci. 262, 930–939.

816 Yue, Y.Z., 2008. Characteristic temperatures of enthalpy relaxation in glass. J. Non. Cryst.
817   Solids 354, 1112–1118. https://doi.org/10.1016/j.jnoncrysol.2006.11.027

818

819